

Dynamical ejecta synchrotron emission as a possible contributor to the rebrightening of GRB170817A

Vsevolod Nedora¹, David Radice^{2,3,4}, Sebastiano Bernuzzi¹, Albino Perego^{5,6},
Boris Daszuta¹, Andrea Endrizzi¹, Aviral Prakash^{2,3}, Federico Schianchi¹,

¹Theoretisch-Physikalisches Institut, Friedrich-SchillerUniversität Jena, 07743, Jena, Germany

²Institute for Gravitation & the Cosmos, The Pennsylvania State University, University Park, PA 16802, USA

³Department of Physics, The Pennsylvania State University, University Park, PA 16802, USA

⁴Department of Astronomy & Astrophysics, The Pennsylvania State University, University Park, PA 16802, USA

⁵Dipartimento di Fisica, Università di Trento, Via Sommarive 14, 38123 Trento, Italy

⁶INFN-TIFPA, Trento Institute for Fundamental Physics and Applications, via Sommarive 14, I-38123 Trento, Italy

Accepted XXX. Received YYY; in original form ZZZ

ABSTRACT

Over the past three years, the fading non-thermal emission from the GW170817 remained generally consistent with the synchrotron afterglow from the forward shock of a relativistic structured jet. Recent observations by [Hajela et al. \(2021\)](#) indicate the emergence of a new component in the X-ray band. We show that the new observations are compatible with a rebrightening due to non-thermal emission from the fast tail of the dynamical ejecta of ab-initio binary neutron star (BNS) merger simulations. This provides a new avenue to constrain binary parameters. Specifically, we find that equal mass models with soft equation of state (EOS) and high mass ratio models with stiff EOS are disfavored as they typically predict afterglows that peak too early to explain observations. Moderate stiffness and mass ratio models, instead, tend to be in good overall agreement with the data.

Key words: neutron star mergers – stars: neutron – equation of state – gravitational waves

1 INTRODUCTION

The GW170817 event marked the dawn of the era of multimessenger astronomy with compact binary mergers. This event was observed as gravitational wave (GW) source, GW170817 ([Abbott et al. 2017a, 2019a,b](#)); quasi-thermal electromagnetic (EM) transient, commonly referred to as kilonova, AT2017gfo ([Arcavi et al. 2017; Coulter et al. 2017; Drout et al. 2017; Evans et al. 2017; Hallinan et al. 2017; Kasliwal et al. 2017; Nicholl et al. 2017; Smartt et al. 2017; Soares-Santos et al. 2017; Tanvir et al. 2017; Troja et al. 2017; Mooley et al. 2018; Ruan et al. 2018; Lyman et al. 2018](#)); and short γ -ray burst (SGRB), GRB170817A ([Savchenko et al. 2017; Alexander et al. 2017; Troja et al. 2017; Abbott et al. 2017b; Nynka et al. 2018; Hajela et al. 2019](#)), detected by the space observatories Fermi ([Ajello et al. 2016](#)) and INTEGRAL ([Winkler et al. 2011](#)). This SGRB was dimmer than any other events of its class. Different interpretations for its dimness and slow rising flux were proposed: off-axis jet, cocoon or structured jet. Now it is now commonly accepted that GRB170817A was a structured jet observed off-axis (*e.g.* [Fong et al. 2017; Troja et al. 2017; Margutti et al. 2018; Lamb & Kobayashi 2017; Lamb et al. 2018; Ryan et al. 2020](#)). The GRB170817A late emission, the afterglow, provided further information on the energetics of the event and on the properties of the circumburst medium (*e.g.* [Hajela et al. 2019](#)).

The non-thermal afterglow of GRB170817A has been observed for over three years, fading after its peak emission at ~ 160 days after merger. At the time of writing, 3.2 years past the merger, the post-jet-break afterglow is still being observed, albeit only in X-ray

by Chandra ([Hajela et al. 2021](#)) and in radio by VLA ([Balasubramanian et al. 2021](#)), as its flux in optical wavelengths has decreased below the detection limit ([Troja et al. 2020](#)). The afterglow flux has been decaying across all frequencies since the jet break ~ 160 days postmerger, with a low-significance, but detectable, flattening in the X-ray, ([Troja et al. 2020](#)). Possible interpretations of this behavior includes changes in the expanding ejecta dynamics due to, *e.g.*, changes in the interstellar medium (ISM) density; variations in microphysical parameters of the shock; or the emergence of a new emission component, *e.g.*, the kilonova afterglow ([Troja et al. 2020](#)). More recent observations by Chandra show a further change in the afterglow behaviour. In particular the X-ray flux has started rising corroborating the emergence of a new emission component ([Hajela et al. 2021](#)). This opens a new avenue for the multimessenger study of GW170817.

In the past few years GW170817 and its EM counterparts have been the subjects of intense investigations and the privileged target for numerical and analytical studies. The wealth of GW models and analysis techniques allowed to constrain the intrinsic parameters of the binary, such as the masses of the merged objects, and the properties of the EOS of cold, beta-equilibrated nuclear matter. The modeling of the kilonova light curves (LCs) and spectra shed new light on the origin of the heaviest elements in the Universe, including lanthanides and actinides ([Barnes et al. 2016; Kasen et al. 2017; Tanaka et al. 2017; Miller et al. 2019; Bulla 2019](#)), and constrained the properties of the matter ejected during the merger, (*e.g.* [Villar et al. 2017; Perego et al. 2017; Siegel 2019; Breschi et al. 2021](#)).

The joint analysis of GW and kilonova emission allowed to further constrain the properties of the binary and of the neutron star (NS) EOS (Margalit & Metzger 2017; Bauswein et al. 2017; Radice et al. 2018a; Dietrich et al. 2018; Radice & Dai 2019; Dietrich et al. 2020; Breschi et al. 2021).

It has long been suggested that the dynamical ejecta from BNS mergers can be the source of a non-thermal, synchrotron emission resulting from the interaction of these ejecta with the surrounding ISM (e.g. Nakar & Piran 2011; Piran et al. 2013; Hotokezaka & Piran 2015). Depending on the binary and EOS properties, numerical relativity (NR) simulations show the presence of fast, mildly relativistic material at the forefront of the dynamical ejecta which can efficiently power this emission. Thus, a non-thermal kilonova afterglow is expected as one of the possible observable EM counterparts of GW170817 (e.g. Hotokezaka et al. 2018; Radice et al. 2018c,b).

In this work we show that the observed X-ray behavior can be explained by an emerging non-thermal afterglow emission from the fast tail of BNS dynamical ejecta. We consider state-of-the-art NR simulations targeted to the GW170817 event (i.e., with GW170817 binary chirp mass) and documented in (Perego et al. 2019; Nedora et al. 2019; Bernuzzi 2020; Nedora et al. 2021). We compute synthetic LCs from the simulated ejecta using semi-analytical methods and show that the peak time and flux are consistent with the recent observations from some of the models. This provides a new avenue to constrain the binary parameters, suggesting that the equal mass models with very soft EOS peak too early to be consistent with observed rebrightening of the GRB170817A X-ray afterglow.

2 BINARY NEUTRON STAR MERGER DYNAMICS AND DYNAMICAL MASS EJECTION

NR simulations of BNS mergers provided a quantitative picture of the merger dynamics, mass ejection mechanisms and remnant evolution (e.g. Shibata & Hotokezaka 2019; Radice et al. 2020; Bernuzzi 2020).

We consider a large set of NR BNS merger simulations targeted to GW170817 (Perego et al. 2019; Endrizzi et al. 2020; Nedora et al. 2019; Bernuzzi et al. 2020; Nedora et al. 2021). These simulations were performed with the GR hydrodynamics code `WhiskyTHC` (Radice & Rezzolla 2012; Radice et al. 2014a,b, 2015), and included neutrino emission and absorption using the M0 method described in Radice et al. (2016) and Radice et al. (2018c), and turbulent viscosity of magnetic origin via an effective subgrid scheme, as described in Radice (2017) and Radice (2020). The impact of viscosity on the dynamical ejecta properties was investigated in Radice et al. (2018b), Radice et al. (2018c), and Bernuzzi et al. (2020), while the importance of neutrinos for determining the ejecta properties was discussed in Radice et al. (2018c) and (Nedora et al. 2021), where it was shown that neutrino reabsorption increases the ejecta mass and velocity – two main quantities for the kilonova afterglow. All simulations were performed using finite temperature, composition dependent nuclear EOSs. In particular, we employed the following set of EOSs to bracket the present uncertainties: DD2 (Typel et al. 2010; Hempel & Schaffner-Bielich 2010), BLh (Logoteta et al. 2020), LS220 (Lattimer & Swesty 1991), SLy4 (Douchin & Haensel 2001; Schneider et al. 2017), and SFHo (Steiner et al. 2013). Among them, DD2 is the stiffest (thus providing larger radii, larger tidal deformabilities and larger NS maximum masses), while SFHo and SLy4 are the softest.

When NSs collide and merger, matter is ejected through a number of different physical processes, gaining enough energy to become

Table 1. Properties of the fast tail of the dynamical ejecta (that has velocity $v > 0.6c$) for a list of NR simulations from Nedora et al. (2021) for which this ejecta is found. Columns, from left to right, are: the EOS, reduced tidal parameter, mass ratio, mass of the fast tail, its mass-averaged electron fraction, and velocity, and the RMS half-opening angle around the binary plane. Asterisk next to EOS indicate a model with subgrid turbulence.

EOS	$\tilde{\Lambda}$	q	M_{ej} [M_{\odot}]	$\langle Y_e \rangle$	$\langle v_{\infty} \rangle$ [c]	$\langle \theta_{\text{RMS}} \rangle$ [deg]
BLh*	541	1.00	1.52×10^{-6}	0.25	0.63	59.55
BLh	541	1.00	2.53×10^{-5}	0.32	0.68	30.05
BLh	539	1.34	1.37×10^{-6}	0.28	0.62	40.73
BLh*	539	1.34	8.02×10^{-7}	0.20	0.63	18.05
BLh	540	1.43	1.19×10^{-8}	0.32	0.60	60.74
BLh*	543	1.54	1.22×10^{-6}	0.31	0.62	61.23
BLh	538	1.66	1.25×10^{-6}	0.32	0.62	51.40
BLh*	532	1.82	6.40×10^{-7}	0.36	0.74	67.44
DD2*	853	1.00	6.65×10^{-6}	0.28	0.63	12.80
DD2	853	1.00	9.65×10^{-7}	0.28	0.63	23.27
DD2*	847	1.20	4.19×10^{-7}	0.24	0.61	20.02
DD2	846	1.22	1.34×10^{-5}	0.26	0.65	16.90
LS220*	715	1.00	1.20×10^{-7}	0.36	0.61	47.76
LS220	715	1.00	3.40×10^{-8}	0.26	0.61	70.38
LS220	714	1.16	1.17×10^{-6}	0.28	0.62	43.90
LS220*	714	1.16	4.33×10^{-6}	0.28	0.63	36.21
LS220*	717	1.11	7.57×10^{-6}	0.35	0.66	43.25
LS220	710	1.43	1.01×10^{-5}	0.37	0.66	76.98
LS220	707	1.66	8.39×10^{-5}	0.38	0.73	52.94
SFHo*	413	1.00	3.97×10^{-5}	0.31	0.67	52.76
SFHo	413	1.00	2.92×10^{-5}	0.30	0.66	53.13
SFHo*	412	1.13	8.40×10^{-5}	0.23	0.69	25.36
SFHo	412	1.13	4.54×10^{-5}	0.29	0.67	31.69
SLy4*	402	1.00	5.13×10^{-5}	0.31	0.67	48.85
SLy4	402	1.00	3.21×10^{-5}	0.30	0.69	44.02
SLy4*	402	1.13	1.70×10^{-4}	0.20	0.67	24.02

gravitationally unbound. In particular, the matter ejected within a few dynamical timescales (i.e., ~ 10 ms) after merger by tidal torques and hydrodynamics shocks driven by core bounces is called dynamical ejecta. It was found that, within the velocity distribution of the dynamical ejecta, some simulations contain also a very fast tail with $v_{\text{ej}} \geq 0.6c$ (Piran et al. 2013; Hotokezaka et al. 2013; Kyutoku et al. 2014; Metzger et al. 2015; Ishii et al. 2018; Hotokezaka et al. 2018; Radice et al. 2018c). The extensive analysis of this tail and its origin in a sample of NR simulations showed that the total mass of this tail depends on the binary parameters and on the NS EOS, but it is typically $\sim 10^{-6} - 10^{-5} M_{\odot}$. This fast tail can be decomposed into two components: the early fast ejecta that are channeled to high latitudes and that originate at the collisional interface of, predominantly, equal mass models with soft EOSs; and the late fast ejecta, that are largely confined to the plane of the binary, and are driven by the shock breakout from the ejecta after the first core bounce (Radice et al. 2018c).

In the following we consider the fast ejecta tail in the set of GW170817 targeted simulations (see above). The ejecta properties are extracted from the simulations at a coordinate radius of $R = 300G/c^2 M_{\odot} \approx 443$ km from the center corresponding to the furthest extraction radius available. This ensures that the ejecta had the longest possible evolution inside the computational domain. This is also consistent with Radice et al. (2018c). The simulations were performed at a standard resolution with a grid spacing at the most refined grid level $\Delta x \approx 178$ m. We also performed several

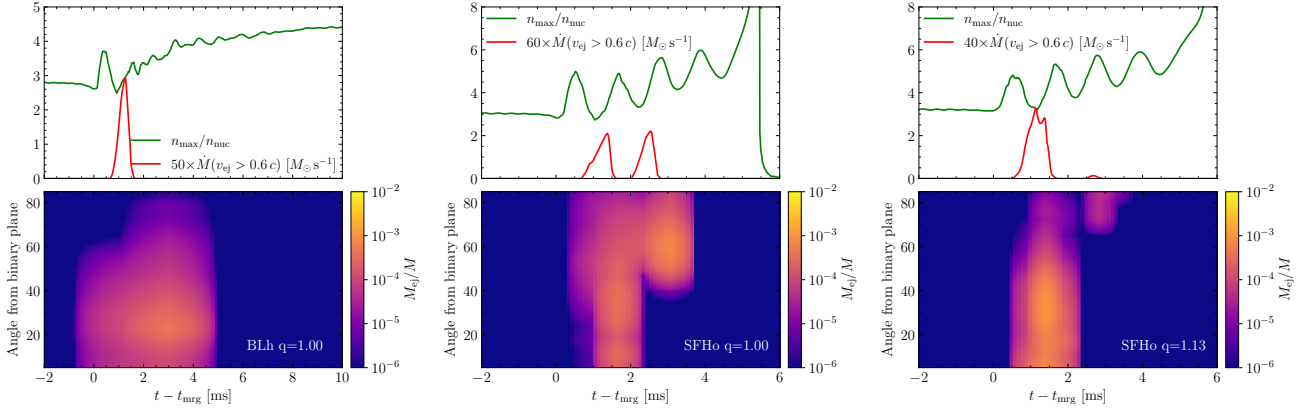


Figure 1. Ejection mechanism and properties of the fast tail of the ejecta shown for three simulations, with two EOSs: BLh and SFHo and two mass ratios: $q = 1.00$ and $q = 1.22$. The upper panel in each plot shows the time evolution of the maximum density in the simulation (green curves) and the mass flux of the ejecta with asymptotic velocities exceeding $0.6c$ (red curve). The bottom panel shows the mass histogram of the fast ejecta tail as a function of time. In both panels the outflow rate and histograms are computed at a radius of $R = 443$ km and shifted in time by $R\langle v_{\text{fast}} \rangle^{-1}$, $\langle v_{\text{fast}} \rangle$ being the mass averaged velocity of the fast tail at the radius R . The plot shows that most of the fast ejecta are generally produced at first core bounce with a contribution from the second in models with soft EOSs.

simulations with higher resolution, $\Delta x \approx 123$ m, to assess the resolution effects on ejecta properties.

Notably, not all simulations are found to host a measurable amount of fast ejecta. Specifically, we find the absence of the fast ejecta component in simulations with stiff EOS and relatively high mass ratio, $q = M_1/M_2 \geq 1$, where M_1 and M_2 are the gravitational masses at infinity of the primary and secondary NSs respectively. The dynamical ejecta velocity distribution from these models shows a sharp cut-off at $\leq 0.5c$. The absence of fast ejecta can be understood from the fact that at large q the ejecta are dominated by the tidal component, whose speed is largely set by the NSs velocities at the last orbit and the system escape velocity. Additionally, our models with large mass ratio (with fixed chirp mass) experience prompt collapse with no core bounce (Bernuzzi et al. 2020).

The production mechanism of the fast ejecta tail is shown in Fig. 1. We find that in our sample of simulations the ejection of mass with velocity $v > 0.6c$ coincides with core bounces, in agreement with previous findings by Radice et al. (2018c). In models with moderately soft EOS or large mass ratio, e.g., the equal mass BLh EOS model or the unequal mass models with softer EOS, e.g., SFHo EOS model, most of the ejecta originate at the first bounce. However, in equal mass models with very soft EOS, e.g., the equal mass SLy4 EOS model, we find that additional mass ejection occurs at the second bounce. Notably, while the first-bounce component is generally equatorial, the second-bounce component is more polar. This might be attributed to the increased baryon loading of the equatorial region resulting from the slow bulk of dynamical ejecta and with the disc forming matter.

The presence of the fast tail is robust and is not affected by resolution. The mass of the fast tail, $M_{\text{ej}}(v > 0.6c)$, however, does have a resolution dependency, and we find that $M_{\text{ej}}(v > 0.6c)$ changes by a factor of a few between simulations at standard and high resolutions. A larger sample of simulations performed at high resolutions is required to assess this uncertainty more quantitatively. The mean value of the fast tail mass is $\overline{M_{\text{ej}}}(v > 0.6c) = (2.36 \pm 3.89) \times 10^{-5} M_{\odot}$, where we also report the standard deviation.

Other properties of the fast tail, such as velocity, electron fraction and angular distribution, are more robust with respect to resolution, similarly to what is observed for the total dynamical ejecta (Nedora

et al. 2021). We report the ejecta properties of simulations performed with standard resolution Tab. 1. We find that for most models, the mass averaged velocity of the fast tails, $v_{\infty}(v > 0.6c)$, is close to $0.6c$ with models with softer EOSs displaying higher velocities. The mass-averaged electron, $Y_e(v > 0.6c)$ is generally above 0.25, indicating that these ejecta were shock-heated and reprocessed by neutrinos. High average electron fraction implies that only weak r -process nucleosynthesis would occur, producing elements up to the 2nd r -process peak (Lippuner & Roberts 2015).

The total kinetic energy of the fast tail, $E_k(v > 0.6c)$, is shown in top panel of the Fig. 2. The error bars cover a conservative ~ 1 order of magnitude, that is obtained by considering the resolution dependency of the fast ejecta mass and velocity, and by assuming the same error measures adopted in Radice et al. (2018c). The figure shows that the total kinetic energy of the fast tail ranges between $\sim 10^{46}$ erg, and $\geq 10^{50}$ erg. Overall, the kinetic energy of the fast tail does not show a strong dependency on the EOS, even if very soft EOSs (like SLy4 and SFHo) tend to have larger energies. The dependency on the mass ratio is more prominent, especially for the SLy4, SFHo and LS220 EOSs, where for the latter, the $E_k(v > 0.6c)$ rises by ~ 3 orders of magnitude between $q = 1$ and $q = 1.7$. Notably, for the BLh EOS models, the total kinetic energy does not change with the mass ratio.

In the lower panel of the Fig. 2 we show the RMS half-opening angle of the fast ejecta around the orbital plane. We assume a conservative error of 5 degrees, motivated by the comparison with higher resolution simulations. As the angular distribution of fast ejecta depends on the ejection mechanism, the figure allows to assess which mechanism dominates in each simulation. The fast ejecta tail is largely confined to the binary plane for the models with stiff EOS, e.g., DD2 EOS, where the core bounce ejection mechanism dominates. Meanwhile, in simulations with soft EOSs and high mass ratios, the fast ejecta has a more uniform angular distribution determined by an interplay between the core dynamics and finite temperature effects driving shocked outflow.

As the mass of the ejecta fast tail shows resolution dependency, so does its total kinetic energy. For three models for which the fast ejecta were found in both the standard and high resolution simulations, we find that $E_{k,\text{ej}}(v_{\text{ej}} > 0.6)$ changes by at least factor of a

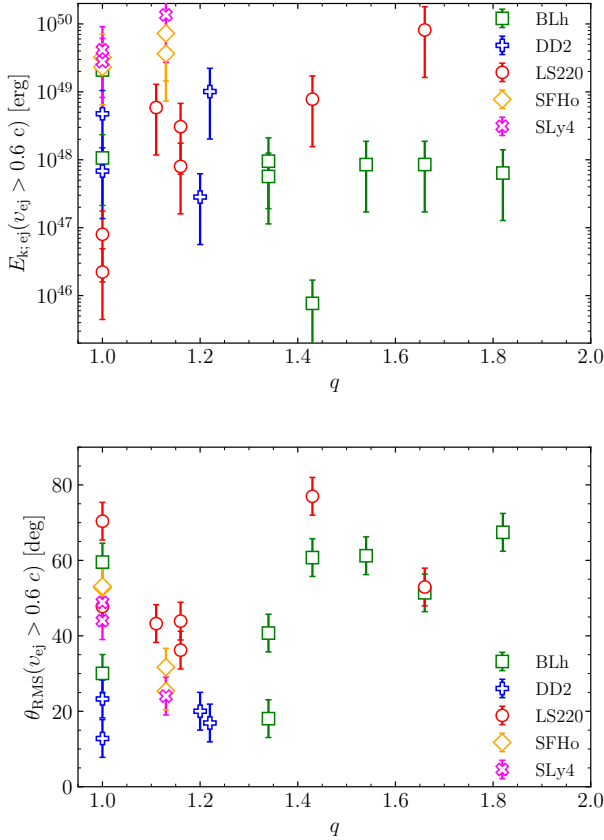


Figure 2. Properties of the fast tail of the dynamical ejecta: total kinetic energy (*top panel*) and half-RMS angle around the binary plane (*bottom panel*) from a selected set of simulations where this tail is present (see text). We assume conservative uncertainties for the angle, 0.5 deg, and half of the value for the kinetic energy. The top panel shows that only for some EOSs the total kinetic energy appear to depend on mass ratio. Specifically, LS220m SFHo and SLy4 EOSs. The half-RMS angle appears to depend more on EOS, and to be overall larger for high- q models.

few. The ejecta RMS half-opening angle about the orbital plane is less resolution dependent and its uncertainty is less than $\sim 50\%$.

Next we consider the distribution of the cumulative kinetic energy of the ejecta, defined as the kinetic energy of the ejecta whose mass is above a certain speed. We express it as a function of the $\Gamma\beta$ product, where β is the ejecta velocity expressed in units of c , and $\Gamma = 1/\sqrt{1-\beta^2}$ is the Lorentz factor. We show $E_k(> \Gamma\beta)$ for representative set of models in Fig. 3. The plot displays that for most models the bulk of the kinetic energy is allocated to the low velocity matter, *i.e.* for $\Gamma\beta \leq 0.5$. Equal mass models show an extended high velocity tail, especially the $q = 1.00$ model with SLy4 EOS. The bottom panel of the Fig. 3 shows the cumulative kinetic energy distribution in terms of the $\beta\Gamma$ product and angle from the plane of the binary for the $q = 1.00$ model with BLh EOS. The distribution is not uniform with respect to the polar angle. While the high energy tail extends up to the polar angle, the high velocity tail is more confined to the orbital plane. Notably, since the largest part (in mass) of the ejecta is equatorial it eludes the interaction with the γ -ray burst (GRB) collimated ejecta and expands into an unshocked ISM. The latter can decrease the ISM density and delay the peak of the synchrotron emission (Margalit & Piran 2020).

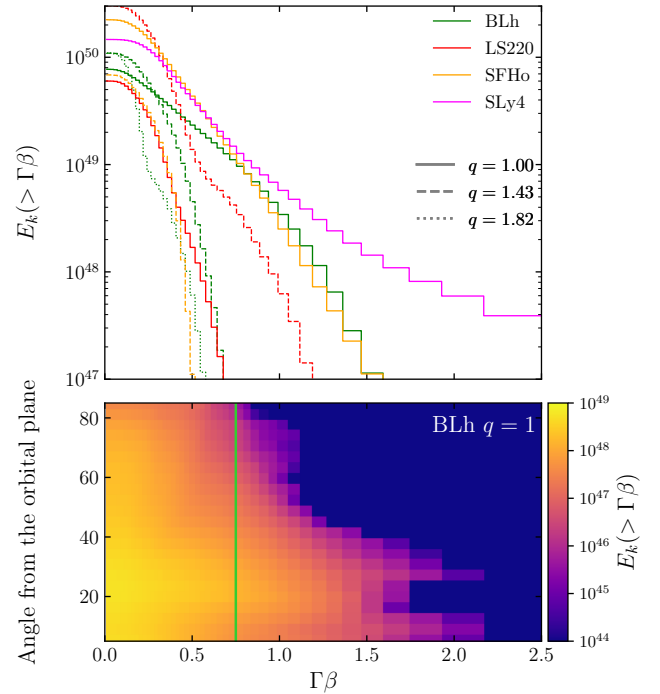


Figure 3. Cumulative kinetic energy distribution for a selected set of models (*top panel*) and its angular distribution for a BLh $q = 1.00$ model (*bottom panel*). The vertical light green line marks the $v_{\text{ej}} = 0.6$. The top panel shows that equal mass models have a more extend high energy tail, while the bottom panel shows that the angular distribution of the ejecta is not uniform.

3 THE SYNCHROTRON EMISSION FROM EJECTA-ISM INTERACTION

Evaluating the synchrotron emission from the merger ejecta requires the calculation of the dynamical evolution of the blast wave as it propagates through the ISM. The dynamical evolution of a decelerating adiabatic blast wave can be described via the self-similar solutions. If the blast wave remains always relativistic, the Blandford-McKee (BM) solution (Blandford & McKee 1976) applies. If the blast wave remains always subrelativistic, the Sedov-Taylor (ST) solution (Sedov 1959) can be used. Another approach to compute the dynamics of the blast wave is to consider the hydrodynamical properties of the fluid behind the shock to be uniform within a given (thin) shell (*e.g.* Pe'er 2012; Nava et al. 2013). This thin homogeneous shell approximation allows to describe the entire evolution of the shell's Lorentz factor from the free coasting phase (where the blast wave velocity remains constant) to the subrelativistic phase. However, there are limitations to this approach. Specifically, it was shown to differ from BM self-similar solution in the ultrarelativistic regime by a numerical factor (Panaitescu & Kumar 2000), and a self-similar solution of the non-relativistic deceleration (Huang et al. 1999). In application to the mildly relativist ejecta with velocity structure, the deviation was shown to be of order unity (Piran et al. 2013; Hotokezaka & Piran 2015).

We calculate the non-thermal radiation arising from the dynamical ejecta propagating into the cold ISM with the semi-analytic code `PyBlastAfterglow`. The method can be summarized as follow-

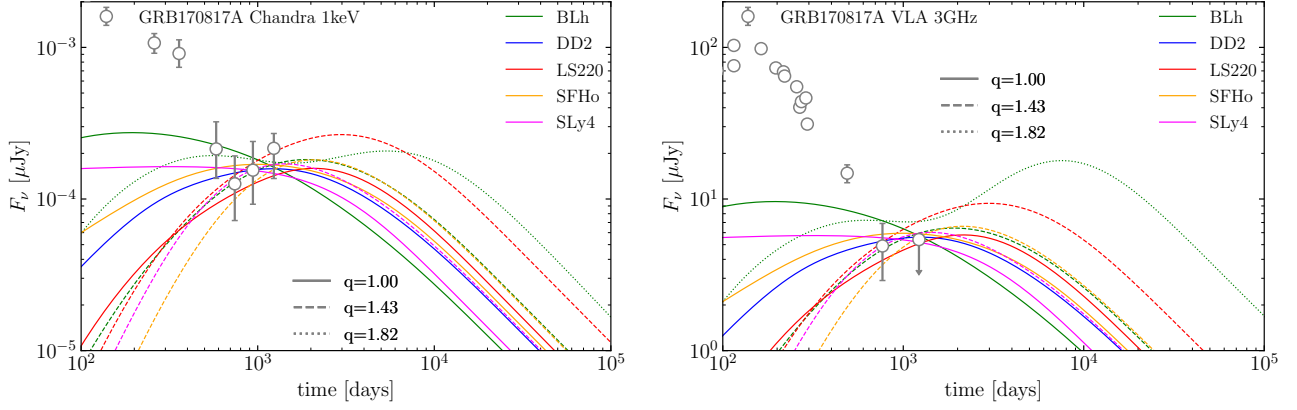


Figure 4. Representative kilonova afterglow LCs for NR models, in X-ray (*left panel*) and in radio (*right panel*), where the gray circles are the observational data (Hajela et al. 2021). The synthetic LCs are computed with varying microphysical parameters and ISM density within the range of credibility to achieve a better fit to observational data (see Tab. 3 for details). The plots show that, within allowed parameter ranges, the LCs from all models are in agreement with observations. Models with moderately stiff EOS and $q < 1 < 1.8$ are tentatively preferred, as their flux is rising at $t \geq 10^3$ days, in agreement with observations.

ing. For a given distribution of energies as a function of velocity, we divide the ejecta into velocity shells and solve the adiabatic radial expansion of the ejecta in the thin shell approximation at each polar angle using the kinetic energy distributions discussed in Sec. 2. See also *e.g.*, Piran et al. (2013) and (Hotokezaka & Piran 2015) for similar treatments.

For the adiabatic evolution we adopt the blast wave dynamics formalism developed by Nava et al. (2013) where the evolution of the blast wave Lorentz factor is given by their equations 3-7, which we solve numerically via a 4th order adaptive step Runge–Kutta (RK) method. We neglect the effects of radiation losses and lateral spreading of the blast wave and focus on its evolution prior to and shortly after the onset of the deceleration. The EOS assumed is that of the ideal transrelativistic fluid, where the adiabatic index is given as a function of the normalized temperature (equation 11 in Pe’er 2012) which is computed adopting the polynomial fit (equation 5 in Serice 1986)

Next, we consider the forward shock propagating into the upstream medium as the blast wave expands. The bulk of the energy is being deposited into the non-thermal protons. Part of this energy is transferred to relativistic electrons via complex shock interactions. It is however possible to consider a simplified prescription for the transfer of energy from protons to electrons (*e.g.* Dermer & Chiang 1998). A fraction ϵ_e and ϵ_B of shock internal energy is assumed to be deposited into the relativistic electrons and magnetic field respectively. The injected electrons are assumed to have a power-law distribution $dN/d\gamma_e \propto \gamma_e^{-p}$, where γ_e is the electron Lorentz factor, p is the spectral index, a free parameter. The critical Lorentz factors of the spectrum are the minimum one, γ_{\min} , and the critical one, γ_c , computed via standard expressions (equations A3 and A4 in Johannesson et al. 2006, respectively). Depending on the ordering of the γ_{\min} and γ_c , two regimes are considered, namely the *fast cooling* regime if $\gamma_{\min} > \gamma_c$, and *slow cooling* regime otherwise (Sari et al. 1998).

The comoving synchrotron spectral energy distribution (SED) is approximated with a smooth broken power law according to Johannesson et al. (2006), and computed with their equations A1 and A7 for the slow cooling regime and their equations A2 and A6 for the fast cooling regime. The characteristic frequencies are obtained from the characteristic Lorentz factors γ_{\min} and γ_c via their equation A5.

Table 2. List of parameters for synthetic LCs shown in the Fig 4 and Fig. 5. For the former the microphysical and ISM density are adjusted model-wise to achieved the good agreement with observations. For the latter, (the last row of the table) the parameters are the same for all models shown. Other parameters, such as observational angle, are the same everywhere (see text).

Fig 4	ϵ_e	ϵ_b	n_{ISM}
BLh q=1.00	0.1	0.003	0.005
BLh q=1.43	0.1	0.005	0.005
BLh q=1.82	0.1	0.01	0.03
DD2 q=1.00	0.1	0.008	0.005
LS220 q=1.00	0.1	0.01	0.006
LS220 q=1.43	0.1	0.002	0.005
SFHo q=1.00	0.1	0.001	0.005
SFHo q=1.43	0.1	0.01	0.006
SLy4 q=1.00	0.1	0.001	0.005
SLy4 q=1.43	0.1	0.006	0.005
Fig. 5	0.2	0.005	0.005

The synchrotron self-absorption is included via flux attenuation (*e.g.* Dermer & Menon 2009). However, for the applications discussed in this paper, the self-absorption is not relevant as the ejecta remains optically thin for the emission ≥ 3 GHz (*e.g.* Piran et al. 2013).

We compute the observed flux, integrating over the equal time arrival surface (EATS), following Lamb et al. (2018). For each segment of the blast wave, the time for the observer is evaluated via their equation 3, and then the observed, Doppler-shifted flux is obtained via their equation 2. See Salmonson (2003) for the detailed discussion of the method and Fernández et al. (2021) for a similar implementation.

In the ultrarelativistic regime, evolving a single velocity shell, the code was found to be consistent with `afterglowpy` (Ryan et al. 2020), while in the subrelativistic regime, modeling the kilonova afterglow, the code produces LCs consistent with the model of Hotokezaka & Piran (2015), which was applied to the BNS ejecta in Radice et al. (2018c). It is however important to note that the methods discussed above for both the blast wave dynamics and the synchrotron emission become increasingly inaccurate as the blast wave decelerates and spreads, and as most of the electrons become subrelativistic. So we do not discuss the late-time emission

after the LC peak. We discuss different physics implemented in `PyBlastAfterglow` with application to both structured GRBs and analytic ejecta profiles elsewhere.

The free parameters of the model are chosen as follows. We assume the ISM density to be uniform within the range $n_{\text{ISM}} \in (10^{-3}, 10^{-2}) \text{ cm}^{-3}$ (Hajela et al. 2019). The observational angle, defined as the angle between the line of sight and the polar axis of the BNS system, is $\theta_{\text{obs}} = 30 \text{ deg}$ (Abbott et al. 2017a). For the luminosity distance of NGC 4993, the host galaxy of GW170817, we adopt $41.3 \times 10^6 \text{ pc}$ with the redshift $z = 0.0099$ (Hjorth et al. 2017).

Recent Chandra observations showed that the emerging component in GRB170817A afterglow is accompanied by the onset of the spectral evolution (Hajela et al. 2021). The observation data analysis suggests that a lower value for the electron power law distribution slope is more favorable, $p = 2.05$, but at low significance level. Due to this uncertainties, we consider the following parameter ranges $\epsilon_e \in (0.1, 0.2)$, $\epsilon_B \in (10^{-3}, 10^{-2})$, and we fix the $p = 2.15$. The effect of a lower $p = 2.05$ is discussed in Hajela et al. (2021).

4 RESULTS

We show X-ray and radio LCs from several representative models in Fig. 4, alongside the latest GRB170817A observational data. The LC shape is determined by the ejecta velocity and angular distribution. For instance, models with broad velocity distribution, such as equal mass model with SLy4 EOS (see Fig. 3), have a wide LC. This LC start to rise very early (in comparison with the high mass ratio model) as the fast velocity shells decelerate and peak on a shorter timescales. However, models with narrower velocity distribution, such as the model with LS220 EOS and $q = 1.43$, have a narrower LC that rises later ($\sim 10^2$ days after merger). Generally, within the uncertain microphysics and ISM density, the kilonova afterglow from most models is in a good agreement with the new observations by Chandra. In particular, models with $1.00 < q < 1.82$ and moderately stiff EOSs show rise in flux $\geq 10^3$ days postmerger, in agreement with observations

Fixing the microphysical parameters and ISM density to $n_{\text{ISM}} = 5 \times 10^{-3} \text{ g cm}^{-3}$, $\epsilon_e = 0.1$ and $\epsilon_b = 5 \times 10^{-3}$, we find that the flux at the LC peak, $F_{\nu,p}$, is the largest for soft EOSs such as SFHo and SLy4. Overall, however, the peak flux seems largely independent of EOS. The $F_{\nu,p}$ dependency on the mass ratio for soft EOSs is that, the higher the mass ratio, the lower the peak flux. This can be understood from the following considerations. While the ejecta total kinetic energy budget of these models increases with the mass-ratio, the mass-averaged velocity decrease (see Fig. 5 in Nedora et al. (2021)). And slower, more massive ejecta have lower peak flux. However, for stiffer EOSs, such as DD2 and LS220, the q dependency is less clear.

The LC shape and the peak time depend weakly on the uncertain microphysics and n_{ISM} . Specifically, within $n_{\text{ISM}} \in (10^{-3}, 10^{-2}) \text{ cm}^{-3}$, t_p varies by a factor of a few. An additional source of uncertainties is the ejecta properties dependency on numerical resolution. However we estimate its effect on the LCs to be smaller than that of the unconstrained shock microphysics and n_{ISM} . Specifically, the t_p changes by a factor of ≤ 2 , and $F_{\nu,p}$ changes withing a factor of ≤ 4 .

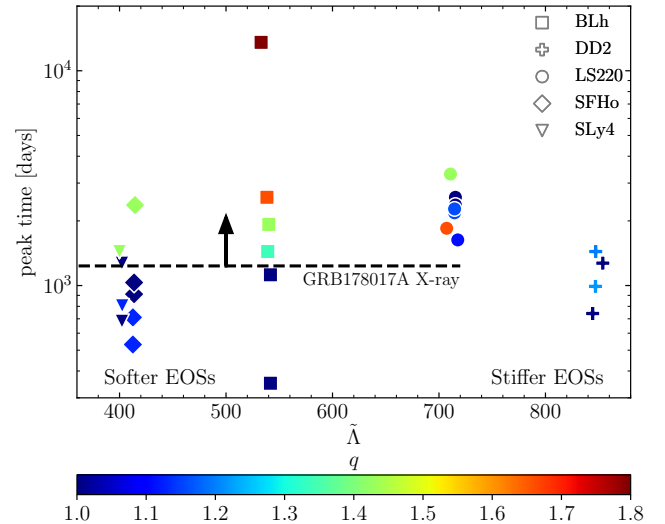


Figure 5. Peak time, t_p , for LC for all considered NR simulations. Dashed black line corresponds to the last observation of GRB170817A afterglow, where the rising flux implies that it is a lower limit on the kilonova afterglow. The microphysical parameters and ISM density for all models are fixed and given in the Tab. 3. The plot shows that in general the t_p increases with mass ratio and with softness of the EOS, except for the softest, DD2 EOS.

5 DISCUSSION

In this work we analyzed a large set of NR BNS simulations performed with state-of-the-art NR code `WhiskyTHC` and targeted to GW170817. Simulations included the effects of neutrino emission and reabsorption, effective viscosity via subgrid turbulence, and microphysical finite-temperature EOSs.

We found that most simulations' ejecta contains material with velocities $\gtrsim 0.6 \text{ c}$, whose properties are in agreement with previous studies (Radice et al. 2018c). However, in binaries with large mass ratio and/or prompt BH formation (that experience weaker/no core bounce at merger), the fast ejecta could be absent.

The latest GRB170817A observations by Chandra at 10^3 days showed a rising flux in X-ray band (Hajela et al. 2021). We suggest that this rebrightening can be attributed to the emergence of the kilonova afterglow. In particular, we evolved the ejecta from NR simulations with a semi-analytic code and computed its synchrotron emission. We found that the synthetic LCs are in agreement with the emerging new component in the GRB170817A afterglow within the range of credibility of the microphysical parameters and of the ISM density, n_{ISM} .

Additionally, the rebrightening has the following implications: the kilonova afterglow peak should be (i) later and (ii) brighter than the latest observations, The condition (ii) is not particularly strong, as the LC peak flux depends sensibly on the uncertain microphysical parameters. The (i) condition is more robust from that point of view and allows to gauge which NR models from our sample have afterglow predictions more supported by observations.

In Fig. 5 we show the time of the LC peak for all models (for fixed microphysics and n_{ISM} , see Tab. 3), including those with absent fast tail, as these models still have sufficient amount of mildly relativistic material to produce a bright afterglow. The time of the synchrotron LC peak, t_p , of all the models is distributed around $\sim 10^3$ days postmerger (except tidal disruption cases, as the model with $q = 1.82$ and BLh EOS). Models with small mass ratio tend

to have $t_p < 10^3$ days, while more asymmetric models point towards $t_p > 10^3$ days. This trend is more apparent for models with soft EOSs. The reason for this lies in the mechanism responsible for the fast ejecta tail (see Sec. 2). As the mass ratio increases, the amount of the shocked ejecta component decreases, and so does the kinetic energy of the ejecta fast tail. The afterglow of the slower, more massive ejecta peaks later (e.g. Hotokezaka & Piran 2015). Indeed, the time of the LC peak depends primarily on the ejecta dynamics, the so-called deceleration time (e.g. Piran et al. 2013). Additionally, in Fig. 5 we show the lower limit on t_p , (the time of the latest observation). We observe that LCs of models with moderate amount of fast ejecta, e.g., asymmetric models with EOSs of mild stiffness, lie above the limit, while models with highly energetic fast tails, such as equal mass models with very stiff EOSs, peak too early.

The main conclusion of our work is that the observed GRB170817A rebrightening at 10^3 days after merger can be explained by the kilonova afterglow produced by ejecta in ab-initio NR BNS simulations targeted to GW170817. Specifically, models that produce a mild amount of fast ejecta, those with moderately to large mass ratio and moderately stiff EOSs are favoured. The dominant uncertainties in our analysis are the ill-constrained microphysical parameters of the shock. Additionally, the systematic effects due to the finite resolution, neutrino treatment and EOSs might be important. A larger set of observations, that allows for a better assessment of shock microphysics, and a larger sample of high resolution NR simulations are required to investigate these uncertainties further. We leave this to future works.

ACKNOWLEDGEMENTS

DR acknowledges support from the U.S. Department of Energy, Office of Science, Division of Nuclear Physics under Award Number(s) DE-SC0021177 and from the National Science Foundation under Grant No. PHY-2011725. S.B., B.D. and F.Z. acknowledge support by the EU H2020 under ERC Starting Grant, no. BinGraSp-714626. Numerical relativity simulations were performed on the supercomputer SuperMUC at the LRZ Munich (Gauss project pn56zo), on supercomputer Marconi at CINECA (ISCRAB project numberHP10BMHFQQ); on the supercomputers Bridges, Comet, and Stampede (NSF XSEDE allocation TG-PHY160025); on NSF/NCSA Blue Waters (NSF AWD-1811236); on ARA cluster at Jena FSU. AP acknowledges PRACE for awarding access to Joliot-Curie at GENCI@CEA, France (project ra5202). This research used resources of the National Energy Research Scientific Computing Center, a DOE Office of Science User Facility supported by the Office of Science of the U.S. Department of Energy under Contract No. DE-AC02-05CH11231. Data postprocessing was performed on the Virgo “Tullio” server at Torino supported by INFN. The authors gratefully acknowledge the Gauss Centre for Supercomputing e.V. (www.gauss-centre.eu) for funding this project by providing computing time on the GCS Supercomputer SuperMUC at Leibniz Supercomputing Centre (www.lrz.de).

REFERENCES

- Abbott B. P., et al., 2017a, *Phys. Rev. Lett.*, 119, 161101
 Abbott B. P., et al., 2017b, *Astrophys. J. Lett.*, 848, L13
 Abbott B. P., et al., 2019a, *Phys. Rev.*, X9, 011001
 Abbott B. P., et al., 2019b, *Phys. Rev.*, X9, 031040
 Ajello M., et al., 2016, *Astrophys. J.*, 819, 44
 Alexander K. D., et al., 2017, *Astrophys. J.*, 848, L21
 Arcavi I., et al., 2017, *Nature*, 551, 64
 Balasubramanian A., et al., 2021
 Barnes J., Kasen D., Wu M.-R., Martínez-Pinedo G., 2016, *Astrophys. J.*, 829, 110
 Bauswein A., Just O., Janka H.-T., Stergioulas N., 2017, *Astrophys. J.*, 850, L34
 Bernuzzi S., 2020, *Gen. Rel. Grav.*, 52, 108
 Bernuzzi S., et al., 2020, *Mon. Not. Roy. Astron. Soc.*
 Blandford R. D., McKee C. F., 1976, *Physics of Fluids*, 19, 1130
 Breschi M., Perego A., Bernuzzi S., Del Pozzo W., Nedora V., Radice D., Vescovi D., 2021
 Bulla M., 2019, *Mon. Not. Roy. Astron. Soc.*, 489, 5037
 Coulter D. A., et al., 2017, *Science*
 Dermer C. D., Chiang J., 1998, *New Astron.*, 3, 157
 Dermer C. D., Menon G., 2009, High Energy Radiation from Black Holes: Gamma Rays, Cosmic Rays, and Neutrinos
 Dietrich T., Bernuzzi S., Bruegmann B., Tichy W., 2018, in 26th Euromicro International Conference on Parallel, Distributed and Network-based Processing. pp 682–689 ([arXiv:1803.07965](https://arxiv.org/abs/1803.07965)), doi:10.1109/PDP2018.2018.00113
 Dietrich T., Coughlin M. W., Pang P. T. H., Bulla M., Heinzel J., Issa L., Tews I., Antier S., 2020, *Science*, 370, 1450
 Douchin F., Haensel P., 2001, *Astron. Astrophys.*, 380, 151
 Drout M. R., et al., 2017, [j 10.1126/science.aag0049](https://doi.org/10.1126/science.aag0049)
 Endrizzi A., et al., 2020, *Eur. Phys. J. A*, 56, 15
 Evans P. A., et al., 2017, [j 10.1126/science.aap9580](https://doi.org/10.1126/science.aap9580)
 Fernández J. J., Kobayashi S., Lamb G. P., 2021
 Fong W., et al., 2017, *Astrophys. J. Lett.*, 848, L23
 Hajela A., et al., 2019, *Astrophys. J. Lett.*, 886, L17
 Hajela A., et al., 2021
 Hallinan G., et al., 2017, [j 10.1126/science.aap9855](https://doi.org/10.1126/science.aap9855)
 Hempel M., Schaffner-Bielich J., 2010, *Nucl. Phys.*, A837, 210
 Hjorth J., et al., 2017, *Astrophys. J. Lett.*, 848, L31
 Hotokezaka K., Piran T., 2015, *Mon. Not. Roy. Astron. Soc.*, 450, 1430
 Hotokezaka K., Kiuchi K., Kyutoku K., Okawa H., Sekiguchi Y.-i., Shibata M., Taniguchi K., 2013, *Physical Review D*, 87, 024001
 Hotokezaka K., Kiuchi K., Shibata M., Nakar E., Piran T., 2018, *Astrophys. J.*, 867, 95
 Huang Y., Dai Z., Lu T., 1999, *Mon. Not. Roy. Astron. Soc.*, 309, 513
 Ishii A., Shigeyama T., Tanaka M., 2018, *Astrophys. J.*, 861, 25
 Johannesson G., Björnsson G., Gudmundsson E. H., 2006, *Astrophys. J.*, 647, 1238
 Kasen D., Metzger B., Barnes J., Quataert E., Ramirez-Ruiz E., 2017, *Nature*
 Kasliwal M. M., et al., 2017, [j 10.1126/science.aap9455](https://doi.org/10.1126/science.aap9455)
 Kyutoku K., Ioka K., Shibata M., 2014, *Mon. Not. Roy. Astron. Soc.*, 437, L6
 Lamb G. P., Kobayashi S., 2017, *Mon. Not. Roy. Astron. Soc.*, 472, 4953
 Lamb G. P., Mandel I., Resmi L., 2018, *Mon. Not. Roy. Astron. Soc.*, 481, 2581
 Lattimer J. M., Swesty F. D., 1991, *Nucl. Phys.*, A535, 331
 Lippuner J., Roberts L. F., 2015, *Astrophys. J.*, 815, 82
 Logoteta D., Perego A., Bombaci I., 2020, [j 10.1051/0004-6361/202039457](https://doi.org/10.1051/0004-6361/202039457)
 Lyman J. D., et al., 2018, *Nat. Astron.*, 2, 751
 Margalit B., Metzger B. D., 2017, *Astrophys. J.*, 850, L19
 Margalit B., Piran T., 2020, [j 10.1093/mnras/staa1486](https://doi.org/10.1093/mnras/staa1486)
 Margutti R., et al., 2018, *Astrophys. J.*, 856, L18
 Metzger B. D., Bauswein A., Goriely S., Kasen D., 2015, *Mon. Not. Roy. Astron. Soc.*, 446, 1115
 Miller J. M., et al., 2019, *Phys. Rev.*, D100, 023008
 Mooley K. P., et al., 2018, *Nature*, 561, 355
 Nakar E., Piran T., 2011, *Nature*, 478, 82
 Nava L., Sironi L., Ghisellini G., Celotti A., Ghirlanda G., 2013, *Monthly Notices of the Royal Astronomical Society*, 433, 2107
 Nedora V., Bernuzzi S., Radice D., Perego A., Endrizzi A., Ortiz N., 2019, *Astrophys. J.*, 886, L30
 Nedora V., et al., 2021, *Astrophys. J.*, 906, 98
 Nicholl M., et al., 2017, *Astrophys. J.*, 848, L18

- Nynka M., Ruan J. J., Haggard D., Evans P. A., 2018, *Astrophys. J. Lett.*, 862, L19
- Panaiteescu A., Kumar P., 2000, *Astrophys. J.*, 543, 66
- Pe'er A., 2012, *The Astrophysical Journal Letters*, 752, L8
- Perego A., Radice D., Bernuzzi S., 2017, *Astrophys. J.*, 850, L37
- Perego A., Bernuzzi S., Radice D., 2019, *Eur. Phys. J.*, A55, 124
- Piran T., Nakar E., Rosswog S., 2013, *Mon. Not. Roy. Astron. Soc.*, 430, 2121
- Radice D., 2017, *Astrophys. J.*, 838, L2
- Radice D., 2020, *Symmetry*, 12, 1249
- Radice D., Dai L., 2019, *Eur. Phys. J.*, A55, 50
- Radice D., Rezzolla L., 2012, *Astron. Astrophys.*, 547, A26
- Radice D., Rezzolla L., Galeazzi F., 2014a, *Class.Quant.Grav.*, 31, 075012
- Radice D., Rezzolla L., Galeazzi F., 2014b, *Mon.Not.Roy.Astron.Soc.*, 437, L46
- Radice D., Rezzolla L., Galeazzi F., 2015, *ASP Conf. Ser.*, 498, 121
- Radice D., Galeazzi F., Lippuner J., Roberts L. F., Ott C. D., Rezzolla L., 2016, *Mon. Not. Roy. Astron. Soc.*, 460, 3255
- Radice D., Perego A., Zappa F., Bernuzzi S., 2018a, *Astrophys. J.*, 852, L29
- Radice D., Perego A., Hotokezaka K., Bernuzzi S., Fromm S. A., Roberts L. F., 2018b, *Astrophys. J. Lett.*, 869, L35
- Radice D., Perego A., Hotokezaka K., Fromm S. A., Bernuzzi S., Roberts L. F., 2018c, *Astrophys. J.*, 869, 130
- Radice D., Bernuzzi S., Perego A., 2020, *Ann. Rev. Nucl. Part. Sci.*, 70, 95
- Ruan J. J., Nynka M., Haggard D., Kalogera V., Evans P., 2018, *Astrophys. J.*, 853, L4
- Ryan G., van Eerten H., Piro L., Troja E., 2020, *Astrophys. J.*, 896, 166
- Salmonson J. D., 2003, *The Astrophysical Journal*, 592, 1002
- Sari R., Piran T., Narayan R., 1998, *Astrophys. J. Lett.*, 497, L17
- Savchenko V., et al., 2017, *Astrophys. J. Lett.*, 848, L15
- Schneider A. S., Roberts L. F., Ott C. D., 2017, *Phys. Rev.*, C96, 065802
- Sedov L. I., 1959, *Similarity and Dimensional Methods in Mechanics*
- Service A. T., 1986, *The Astrophysical Journal*, 307, 60
- Shibata M., Hotokezaka K., 2019, *Ann. Rev. Nucl. Part. Sci.*, 69, 41
- Siegel D. M., 2019, *Eur. Phys. J. A*, 55, 203
- Smartt S. J., et al., 2017, *Nature*
- Soares-Santos M., et al., 2017, *Astrophys. J.*, 848, L16
- Steiner A. W., Hempel M., Fischer T., 2013, *Astrophys. J.*, 774, 17
- Tanaka M., et al., 2017, *Publ. Astron. Soc. Jap.*
- Tanvir N. R., et al., 2017, *Astrophys. J.*, 848, L27
- Troja E., et al., 2017, *Nature*
- Troja E., et al., 2020, *Mon. Not. Roy. Astron. Soc.*, 498, 5643
- Typel S., Ropke G., Klahn T., Blaschke D., Wolter H. H., 2010, *Phys. Rev.*, C81, 015803
- Villar V. A., et al., 2017, *Astrophys. J.*, 851, L21
- Winkler C., Diehl R., Ubertini P., Wilms J., 2011, *Space Science Reviews*, 161, 149